The effect of the magnetically dead layer on the magnetization and the magnetic anisotropy of the dextran-coated magnetite nanoparticles

Zhila Shaterabadi[1,2], Gholamreza Nabiyouni[1,2*], Gerardo F Goya[3], Meysam Soleymani[4]

1. Department of Physics, Faculty of Science, Arak University, Arak, 38156-88349, Iran
2. Institute of Nanoscience and Nanotechnology, Arak university, Arak, Iran
3. Condensed Matter Physics Department, and Instituto de Nanociencias y Materiales de Aragón, Universidad de Zaragoza, C/ Mariano Esquillor s/n, Zaragoza 50018, Zaragoza, Spain
4. Department of Chemical Engineering, Faculty of Engineering, Arak University, Arak, 38156-88349, Iran

Abstract

We present a study on the magnetic behavior of dextran-coated magnetite nanoparticles (DM NPs) with sizes between 3 and 19 nm, synthesized by hydrothermal-assisted co-precipitation method. The decrease of saturation magnetization ($\mathrm{M_s}$) with decreasing particle size has been modeled by assuming the existence of a spin-disordered layer at the particle surface, which is magnetically dead. Based on this core-shell model and taking into account the weight contribution of non-magnetic coating layer (dextran) to the whole magnetization, the dead layer thickness (t) and saturation magnetization $\mathrm{M_s}$ of the magnetic cores in our samples were estimated to be $\mathrm{t} = 6.8$ Å and $\mathrm{M_s} = 98.8\ \mathrm{emu/g}$, respectively. The data of $\mathrm{M_s}$ were analyzed using a law of approach to saturation, indicating an increase in effective magnetic anisotropy ($\mathrm{K_{eff}}$) with decreasing the particle size as expected from the increased surface/volume ratio in small MNPs. The obtained $\mathrm{K_{eff}}$ values were successfully modeled by including an extra contribution of dipolar interactions due to the formation of chain-like clusters of MNPs. The surface magnetic anisotropy ($\mathrm{K_s}$) was estimated to be about $\mathrm{K_s} = 1.04 \times 10^5\ \mathrm{J/m^3}$. Our method provides a simple and accurate way to

---

[*] Corresponding author. E-mail address: g-nabiyouni@araku.ac.ir

obtain the M_s core values in surface-disordered MNPs, a relevant parameter required for magnetic modeling in many applications.

Keywords: Effective magnetic anisotropy; Dipolar interactions; Magnetic dead layer; Core-shell model; Spin disorder; Surface magnetic anisotropy; Dextran-coated magnetite NPs.

1. Introduction

Particle size reduction to the nanometer scale significantly affects magnetic properties of magnetic nanoparticles (MNPs) due to deleterious impact of surface atoms on the effective magnetization of the MNPs [1, 2]. However, when optimal performance is sought in bio-applications such as magnetic hyperthermia therapy [3, 4], drug delivery [5, 6], and magnetic resonance imaging [7, 8], it is important to retain the magnetization values M at room temperature as close as possible to the corresponding bulk ones [9, 10]. Hence, it is important to address size-dependent changes of magnetic properties in nanometer-scaled particles.

As the size of the MNPs decreases below the micrometer-size range several new phenomena appear, including superparamagnetism [11, 12], reduced saturation magnetization [13, 14], and non-saturated and open hysteresis loop at high magnetic fields [15, 16]. For a given material with effective magnetic anisotropy K_{eff}, the superparamagnetic behavior appears when the particle volume V is small enough that the thermal energy can overcome the anisotropy energy barrier $E = K_{eff} V$ separating magnetization easy axes [17, 18]. On the other hand, the reduced and non-saturating magnetization phenomena originate from spin-disordered configuration at the MNP surface, that can be explained by the core-shell model.

This core-shell configuration on MNPs consists of a spin-disordered shell, known as magnetic dead layer (due to its zero net magnetization), surrounding a core with ferro/ferri magnetic-ordered spins [19, 20]. Deterioration of magnetic order in the dead layer is originated from the surface effects in this region. In fact, structural distortions at the MNPs boundaries result in breaking atomic bonds and consequently frustrating exchange interactions between surface and core spins, which in turn lead to the orientation deviation of surface spins with respect to the core ones [19, 21-24]. In ferrites, like magnetite, exchange interactions occur through intermediation of oxygen ions (called super-exchange interactions), and therefore the presence of defects and impurities in surface sites or missing of oxygen ions can spread the spin-disordered region into the core [21-23].

Consequently, the decrease in M_S with the size reduction, which is one consequence of surface effects, has well been described by considering a model in which the MNPs are composed with a core having bulk-like magnetic properties and a surrounding shell composed of a magnetically disordered layer. In fact, as the particle size decreases the impaired magnetic order of the surface layer increasingly determines the magnetic properties of a given MNP. For iron oxide NPs with 0.9 nm magnetic dead layer thickness, Kim et al. reported that 61.4% of spins in 12 nm-sized MNPs are magnetically disordered, while the figure increasingly reaches 99.4% in 2.2 nm-sized MNPs [25]. In addition, the decreasing trend of M_S with the size reduction has been reported in many articles [26-33]. Nevertheless, to the best of our knowledge, there aren't any experimentally-estimated values for the magnetic dead layer thickness of the magnetite NPs with considering the coating ligand-related effect on the measured magnetization.

Several methods have been introduced to synthesize different types of nano-scaled particles, including co-precipitation, hydrothermal, solid state, microwave, microemulsion, and thermal decomposition [34-41]. Among them, co-precipitation method in combination with hydrothermal process is one of the low-cost and most common techniques for preparation of size-controlled MNPs. In this work, the effect of size reduction on the magnetization behavior of variable-sized DM NPs (from 3.1 to 18.9 nm), synthesized by hydrothermal-assisted co-precipitation method, were investigated. Specifically, the magnetic dead layer thickness of DM NPs using real values of M_s at high magnetic fields for the magnetic part of DM NPs were estimated by eliminating the weight contribution of non-magnetic coating layer to the whole magnetization. The K_{eff} values were obtained using a law of approach to saturation were, for the first time, modeled by including an extra contribution of dipolar interactions due to the formation of particle clusters with chain-like structure. The obtained results can provide new insight into the modification of magnetic properties of MNPs, especially for applications in which an accurate determination of M_s is required.

2. Material and methods

2.1. Materials

Ferrous and ferric salts ($FeCl_2 \cdot 4H_2O$ and $FeCl_3 \cdot 6H_2O$), sodium hydroxide, and dextran (Mw≈ 10 KDa) were purchase from Sigma Aldrich company. All chemicals were in the analytical grade, and were used without any further purification.

2.2. Synthesis of DM NPs

The DM NPs were synthesized by combination of co-precipitation and hydrothermal methods. The detail of experimental procedure is given elsewhere [42]. Briefly, co-precipitation of iron salts

($FeCl_2 \cdot 4H_2O$ and $FeCl_3 \cdot 6H_2O$ with molar ratio of 1:2) in the presence of dextran was performed under nitrogen atmosphere and vigorous stirring at 80°C by raising pH to 12 and then stabilizing the conditions for 1 h. The hydrothermal process was also implemented on the resultant black suspension at different aging temperatures from 120°C to 220°C. The synthesis conditions of seven prepared samples are summarized in Table 1.

2.3. Characterization

The X-ray diffraction (XRD) patterns of samples were obtained by the powder X-ray diffraction (XRD, Philips, X-pert) with the Cu-K_α radiation. The morphology and particle size of the samples were investigated by the transmission electron microscopy (TEM, Phylips-CM120) and field emission scanning electron microscopy (FESEM, ZEISS, SIGMA VP). The changes of residual mass with temperature were investigated under nitrogen atmosphere (30-900°C) by TG analysis and using Perkin Elmer instrument. The magnetic properties of the samples were evaluated at room temperature by a vibrating sample magnetometer (VSM, Meghnatis Kavir Kashan Co., Iran) instrument.

3. Results and discussion

The TEM images of the DM NPs are shown in Fig. 1. The corresponding size distribution histograms, obtained by measuring over more than 500 NPs from different pictures, and the lognormal fits are also shown in the inset of each image. The obtained average particle sizes are listed in the Table 1. As can be seen, the average sizes of the DM NPs increase by raising the aging temperature in the hydrothermal process. To provide a better characterization, the morphology of DM19 NPs was also investigated by the FESEM analysis and the result is shown in Fig. 2.

The crystal structure of the samples was determined by XRD analysis and the results are shown in Fig. 3. All reflection peaks in the XRD patterns are in accordance with characteristic peaks (220), (311), (400), (422), (511), (440), (620), and (533) of the cubic spinel structure of Fe_3O_4 (JCPDS Card No. 75-0449), confirming the formation of the pure magnetite phase in our samples. Moreover, the diffraction peaks steadily become sharper and more intense from the DM3 to DM19 sample as a result of the particle size enhancement, in agreement with TEM results.

The hysteresis loops of DM NPs were obtained by VSM analysis and the saturation magnetization values (M_s) are summarized in Table 1. We note that our largest applied field in VSM measurements could be insufficient for complete saturation of samples, and thus the M_s^* values were estimated using extrapolation of magnetization (M) versus the inverse of magnetic field strength ($\frac{1}{H}$) curves. To this end, initial magnetization curves of DM NPs (shown in Fig. 4) were utilized to make M vs. $\frac{1}{H}$ curves using their data near saturation. Both the M_s^* and M_s values are presented per unit of total mass (g_{Dex-M}) which comprises the mass of magnetite NPs (g_{Mag}), dextran layer, and absorbed water on NPs surface. Therefore, M_s^{**} values (real saturation magnetizations at high magnetic filed strengths for pure magnetite NPs) were estimated using effective magnetic material mass obtained by remanence weight (m_r) in TG analyses. The values of M_s^*, and $M_s^{**}$are also summarized in the Table 1. As it can be seen, M_s^{**} values are smaller than those of the bulk material in the range $92-100$ emu/g [17, 43-45]. Moreover, they dramatically decrease with the particle size reduction.

Decline in the saturation magnetization with decrease in the particle size, which has already been observed in other experimental works [46-50], can be originated both from redistribution of cations between two sub-lattices of spinel structure and spin disorder on the particle surface. It has been reported that the distribution of cations between tetrahedral and octahedral sites of spinel structure can significantly affect the magnetization of ferrite NPs [76]. Magnetite (Fe_3O_4) is an interesting member of the spinel ferrite family with inverse structure as $(Fe^{3+})(Fe^{2+}Fe^{3+})O_4$ in which the parentheses indicate the tetrahedral and octahedral sites, respectively [4,76]. Considering the magnetic moments of Fe^{3+} and Fe^{2+} ions as 5 and 4 μ_B respectively, the net magnetic moment of each magnetite molecule is simply calculated as 4 μ_B. Assuming the probable redistribution of a fraction (x) of cations, a partially deviated inverse spinel structure as $(Fe^{2+}{}_{x}Fe^{3+}{}_{1-x})(Fe^{2+}{}_{1-x}Fe^{3+}{}_{1+x})O_4$ with the net magnetic moment $(4 + 2x)$ μ_B is formed [51]. Accordingly, even if the size reduction causes a change in the arrangement of cations in the spinel structure of the magnetite NPs, magnetization is expected to increase. In other words, the magnetization reduction can exclusively be attributed to the existence of the magnetically inert layer on the surface of the MNPs in the core-shell model.

Assuming that the magnetic dead layer has a) a negligible net magnetization and b) a thickness, t, independent of particle size, D, the saturation magnetization M_s is given by

$$M_s = M_{s0}\,(1 - 2t/D)^3 \qquad (1)$$

where M_{s0} is the saturation magnetization of bulk material. Eq.(1) indicates that the decrease of our experimental values of M_s^{**} (i.e., the magnetization corrected for the dextran mass) should be most relevant for the smallest MNPs. The plot of ${M_s}^{**1/3}$ vs. $\frac{1}{D}$ data (Fig. 5) could be well fitted by a linear function as expected from Eq. (1), obtaining the values of $M_{s0} = 98.8\ \text{emu/g}$ and $t = 6.8$ Å for the bulk saturation magnetization and dead layer thickness, respectively ($R^2 = 0.9662$).

The M_{s0} obtained from the fit is consistent with reported values of bulk magnetite $92 - 100\ \text{emu/g}$ [17, 43-45]. The value of the thickness $t = 6.8$ Å obtained from the fit is somewhat smaller than the Fe_3O_4 lattice constant (8.39 Å) [52] but comparable to previous findings $t = 6$ Å found by Chen et al. [53], and Zheng et al. [54] for $MnFe_2O_4$ NPs at 300 K. Other t values consistent with our findings have been reported in different systems, including values of $t = 5$Å (at 10 K) [53], and 4.5 Å (at 20 K) [55] for $MnFe_2O_4$ MNPs, and 10 Å (at 5 K) for $CoFe_2O_4$ NPs [56]. Interestingly, $CuFe_2O_4$ NPs with sizes from 10 to 60 nm produced by mechanical milling were reported to have a much larger $t \approx 2.5$ nm spin-disordered layer thickness, consistent with the high-energy collisions during mechanosynthesis [57]. The only measured values for the bulk saturation magnetization M_{s0} and thickness t in Fe_3O_4 MNPs, to the best of our knowledge, have been reported by Caruntu et al. to be $M_{s0} = 88.65$ emu/g and $t = 2.26$ Å at 300 K [58]. These values are smaller than the estimation values presented here because they have obtained from the plot of M_s vs. $\frac{1}{D}$ data using the equation $M_s = M_{s0}\,(1 - 6t/D)$ which is the expansion of Eq.1. However, comparison between samples obtained from different synthesis routes can be misleading, since the thickness of the disordered surface is expected to depend on the details of the energy landscape involved in each synthesis route. We also note that the thickness t obtained from the extrapolation method could be affected by the M_s values assumed for the magnetic core at high magnetic filed. Our estimations are based on considering the M_s^{**} values obtained from the extrapolation of M vs. $\frac{1}{H}$ curves and the TG results.

Using the obtained t value and assuming the spherical shape for the DM NPs, the magnetic-disordered content for the DM3 NPs was calculated to be 82.3%. It means that the magnetic order only exists in 17.7% of the particle volume. By increasing the particle size, the magnetic-ordered content increases to 79.9% for the DM19 NPs. Therefore, the effect of surface magnetic disorder on the magnetic behavior of MNPs significantly diminishes with increasing the particle size, consistent with the decrease of the surface/volume ratio as the particle size increases.

The magnetization data as a function of the applied field H can be analyzed in terms of the law of approach to saturation [59]:

$$M = M_S \left(1 - \frac{b}{H^2}\right) \qquad (2)$$

where the parameter b is related to the magnetocrystalline anisotropy, which can be obtained from the M(H) data near saturation by a linear fitting of the $\frac{M}{M_S}$ (or $\frac{M^{**}}{M_S^{**}}$ in our assumption) versus $1/H^2$ curve. Following the procedure reported in [60], we calculated K_{eff} for a uniaxial magnetic anisotropy by Eq. (3) [61, 62].

$$K_{eff} = \mu_0 M_S \left(\frac{15}{4} b\right)^{1/2} \qquad (3)$$

Using the b values obtained from Eq. (2) and the M_S^{**} values from Table 1, Eq. (3) yielded the K_{eff} values for DM NPs listed in Table 2. These calculated values are higher than the bulk anisotropy constant ($K_{bulk\ magnetite} = 1.35 \times 10^4\ J/m^3$ [63]), reflecting the surface effects as particle size decreases. This size dependence is consistent with previous findings in iron oxide NPs [58, 60, 63, 64] that reported a rising trend for K_{eff} with size reduction. The size dependency of the K_{eff} is in good agreement with previous results on spherical Fe_3O_4 MNPs showing a decrease in K_{eff} from $4.74 \times 10^5\ J/m^3$ to $1.11 \times 10^5\ J/m^3$ with increasing particle size from 6 to 11 nm [58]. Similar changes in the K_{eff} for cubic magnetite NPs have been observed, with a reduction from $77 \times 10^3\ J/m^3$ (20 nm diameter) to $42 \times 10^3\ J/m^3$ (40 nm diameter) [60]. Sarkar and Mandal also reported a decreasing trend in the K_{eff} from $1.84 \times 10^5\ J/m^3$ (7.23 nm diameter) to $1.25 \times 10^5\ J/m^3$ (11 nm diameter) for chain-like magnetite NPs [63].

Assuming that the magnetocrystalline anisotropy K_{bulk} of the magnetic cores is constant along our series of samples with different particle sizes, additional contributions to the *effective* magnetic anisotropy K_{eff} come from shape and/or surface anisotropies as well as magnetic dipolar interactions among MNPs [65-67]. Since the overall shape of our MNPs does not change significantly along the series of samples as observed from TEM images [42], the contributions from shape anisotropy to K_{eff} can be ignored. The interactions between particles include exchange and dipole-dipole interactions. Exchange interactions act only between particles in contact. Since the dextran-coating makes the MNPs to be separated by at least a distance twice the coating layer thickness, such interactions are no considerable in our system [58, 68, 69]. On the other hand, our experimental determination of the evolution in both K_{eff} and K_S was made on non-diluted samples, so dipolar magnetic interparticle interactions could not be negligible in the analysis of the single-particle magnetic anisotropy. Additionally, since the M_s values in our MNPs decrease with decreasing particle size (see Table 1) the same trend is to be expected for the strength of dipole-dipole interactions.

The phenomenological expression for the anisotropy K_{eff} originally proposed by Bødker et al. [70] as Eq. (4),

$$K_{eff}V \cong K_{bulk}V + K_sS \qquad (4)$$

where K_{bulk} is the bulk anisotropy energy per unit volume, and K_s is the surface density of anisotropy energy. Assuming that the particles are spherical with diameter D, Bødker et al. simplified the Eq. (4) as Eq. (5) which has experimentally been found on many different systems [71, 72].

$$K_{eff} \cong K_{bulk} + \frac{6K_s}{< D >} \qquad (5)$$

Using symmetry arguments and assuming that surface anisotropy is normal to the particle surface, Bødker et al. [70] showed that for a perfectly spherical particle a zero contribution from surface anisotropy should be expected. We note here that this is an empirical expression, and the hypothesis that the surface contribution to the effective anisotropy is simply additive has yet to be demonstrated.

Fig. 6 (a) shows fitting the K_{eff} vs. 1/D data using Eq. (5), from which a value $K_s = 2.11 \times 10^5\ J/m^3$ was obtained for our DM NPs samples. However, as clearly seen in Fig. 6 (a), there is a large deviation from the linear behaviour for large 1/D values. These deviations could be explained by deviations from spherical shape that are not included in Eq. (5). Indeed, for different particle morphologies, Eq. (4) should include an additional contribution with a different K_{eff} vs. 1/D slope. However, as previously mentioned no major change in MNPs overall morphology can be observed in our series of size-increased samples, despite using the hydrothermal route [42].

It should be noted that the original work by Bødker et al., did not consider any contributions from dipolar interactions to the collective behavior of nanoparticles. It is well known that dipolar interactions between MNPs favor the formation of the chain-like clusters in large enough MNPs for which the magnetic dipole-dipole interaction energy can surpass the thermal energy even at room temperature [60, 73-77]. To include these interactions, we modified Eq. 4 and Eq. 5 including a parabolic term:

$$K_{eff} \cong K_{bulk} + \frac{6K_s}{< D >} + \frac{E_l}{< D^2 >} \qquad (6)$$

in which E_l has the unit of a linear density of anisotropy energy. Fig. 6 (b) clearly shows that using Eq. (6) the fit of experimental data can be extended to the full range of particle sizes. The last term in Eq. (6) could be understood as originated from the formation of one-dimensional chains of MNPs (i.e. head-to-tail orientation) due to dipolar interactions. Consistent with Eq. (6) the last term is more relevant for larger 1/D values, reflecting the fact that clustering and chain formation is favoured for larger MNPs due to their larger dipolar moment. These interactions originate the extra contribution to the anisotropy in the Eq. (6) and, with this assumption and using Eq. (6) to fit the K_{eff} vs. 1/D data, a value of $K_s = 1.04 \times 10^5\ J/m^3$ was obtained for our DM NPs samples. The obtained value shows that surface anisotropy gives an important contribution to the effective anisotropy of small MNPs. In fact, surface anisotropy originates from the lack of long-range crystalline order in surface layer where breaking the crystal structure symmetry due to the lower and more variable coordination of cations results in perturbation in crystal field and consequently modification of magnetocrystalline anisotropy [21, 23].

2. Conclusion

We have successfully used a series of magnetite (Fe_3O_4) nanoparticles increasing sizes from 3.1 to 18.9 nm to investigate size-dependent changes in their magnetic properties. Our results revealed that the decrease in the saturation magnetization M_s with decreasing size can be explained by a magnetically-disordered surface layer, and fitting the experimental data the values of the magnetic dead layer thickness and M_s were estimated as $t = 6.8$ Å and $M_s = 98.8\ emu/g$, respectively. We used a modified relation for calculating the contribution of the surface anisotropy K_S to the effective anisotropy K_{eff} by adding the contributions from dipolar interactions to the original model proposed by Bødker et al., obtaining a good fit for the whole range of MNPs sizes. Our analysis provides a clearer picture of the effects of the spin-disordered surface configuration on the magnetic properties in MNPs of diverse sizes.

Acknowledgements

This work has been supported by Arak University Research Council (AURC) and Iran National Science Foundation (INSF). The authors acknowledge AURC and INSF for the financial support.

Conflict of interest

The authors declare that they have no conflict of interest.

References

[1] Issa, B., Obaidat, I.M., Albiss, B.A. and Haik, Y., Magnetic nanoparticles: surface effects and properties related to biomedicine applications. *International journal of molecular sciences*, **2013**, *14*, 21266-21305.

[2] Xi, S.B., Lu, W.J., Wu, H.Y., Tong, P. and Sun, Y.P., Surface spin-glass, large surface anisotropy, and depression of magnetocaloric effect in $La_{0.8}Ca_{0.2}MnO_3$ nanoparticles. *Journal of applied physics*, **2012**, *112*, p.123903.

[3] Reyes-Ortega, F., Delgado, Á.V. and Iglesias, G.R., Modulation of the Magnetic Hyperthermia Response Using Different Superparamagnetic Iron Oxide Nanoparticle Morphologies. *Nanomaterials*, **2021**, *11*, p.627.

[4] Soleymani, M., Velashjerdi, M., Shaterabadi, Z. and Barati, A., One-pot preparation of hyaluronic acid-coated iron oxide nanoparticles for magnetic hyperthermia therapy and targeting CD44-overexpressing cancer cells. *Carbohydrate polymers*, **2020**, *237*, p.116130.

[5] Asgari, M., Soleymani, M., Miri, T. and Barati, A., Design of thermosensitive polymer-coated magnetic mesoporous silica nanocomposites with a core-shell-shell structure as a magnetic/temperature dual-responsive drug delivery vehicle. *Polymers for Advanced Technologies*, **2021**, 1-9.

[6] Oltolina, F., Peigneux, A., Colangelo, D., Clemente, N., D'Urso, A., Valente, G., Iglesias, G.R., Jiménez-Lopez, C. and Prat, M., Biomimetic magnetite nanoparticles as targeted drug nanocarriers and mediators of hyperthermia in an experimental cancer model. *Cancers*, **2020**, *12*, p.2564.

[7] Soleymani, M., Khalighfard, S., Khodayari, S., Khodayari, H., Kalhori, M.R., Hadjighassem, M.R., Shaterabadi, Z. and Alizadeh, A.M., Effects of multiple injections on the efficacy and cytotoxicity of folate-targeted magnetite nanoparticles as theranostic agents for MRI detection and magnetic hyperthermia therapy of tumor cells. *Scientific reports*, **2020**, *10*, 1-14.

[8] Dong, P., Zhang, T., Xiang, H., Xu, X., Lv, Y., Wang, Y. and Lu, C., Controllable synthesis of exceptionally small-sized superparamagnetic magnetite nanoparticles for ultrasensitive MR imaging and angiography. *Journal of Materials Chemistry B*, **2021**, *9*, 958-968.

[9] Cole, A.J., David, A.E., Wang, J., Galbán, C.J., Hill, H.L. and Yang, V.C., Polyethylene glycol modified, cross-linked starch-coated iron oxide nanoparticles for enhanced magnetic tumor targeting. *Biomaterials*, **2011**, *32*, 2183-2193.

[10] Shaterabadi, Z., Nabiyouni, G. and Soleymani, M., Physics responsible for heating efficiency and self-controlled temperature rise of magnetic nanoparticles in magnetic hyperthermia therapy. *Progress in biophysics and molecular biology*, **2018**, *133*, 9-19.

[11] Fonseca, F.C., Goya, G.F., Jardim, R.F., Muccillo, R., Carreno, N.L.V., Longo, E. and Leite, E.R., Superparamagnetism and magnetic properties of Ni nanoparticles embedded in SiO_2. *Physical Review B*, **2002**, *66*, p.104406.

[12] Espinola-Portilla, F., Serrano-Torres, O., Hurtado-López, G.F., Sierra, U., Varenne, A., d'Orlyé, F., Trapiella-Alfonso, L., Gutiérrez-Granados, S. and Ramírez-García, G., Superparamagnetic iron oxide nanoparticles functionalized with a binary alkoxysilane array and poly (4-vinylpyridine) for magnetic targeting and pH-responsive release of doxorubicin. *New Journal of Chemistry*, **2021**, *45*, 3600-3609.

[13] Köhler, T., Feoktystov, A., Petracic, O., Kentzinger, E., Bhatnagar-Schöffmann, T., Feygenson, M., Nandakumaran, N., Landers, J., Wende, H., Cervellino, A. and Rücker, U., Mechanism of magnetization reduction in iron oxide nanoparticles. *Nanoscale*, **2021**, *13*, 6965-6976.

[14] Lima Jr, E., Brandl, A.L., Arelaro, A.D. and Goya, G.F., Spin disorder and magnetic anisotropy in Fe 3 O 4 nanoparticles. *Journal of Applied Physics*, **2006**, *99*, p.083908.

[15] Kale, A., Gubbala, S. and Misra, R.D.K., Magnetic behavior of nanocrystalline nickel ferrite synthesized by the reverse micelle technique. *Journal of Magnetism and Magnetic Materials*, **2004**, *277*, 350-358.

[16] Asiri, S., Sertkol, M., Güngüneş, H., Amir, M., Manikandan, A., Ercan, İ. and Baykal, A., The temperature effect on magnetic properties of $NiFe_2O_4$ nanoparticles. *Journal of Inorganic and Organometallic Polymers and Materials*, **2018**, *28*, 1587-1597.

[17] Kandasamy, G. and Maity, D., Recent advances in superparamagnetic iron oxide nanoparticles (SPIONs) for in vitro and in vivo cancer nanotheranostics. *International journal of pharmaceutics*, **2015**, *496*, 191-218.

[18] Ramimoghadam, D., Bagheri, S. and Abd Hamid, S.B., Progress in electrochemical synthesis of magnetic iron oxide nanoparticles. *Journal of Magnetism and Magnetic Materials*, **2014**, *368*, 207-229.

[19] Curiale, J., Granada, M., Troiani, H.E., Sánchez, R.D., Leyva, A.G., Levy, P. and Samwer, K., Magnetic dead layer in ferromagnetic manganite nanoparticles. *Applied Physics Letters*, **2009**, *95*, p.043106.

[20] Muroi, M., Street, R., McCormick, P.G. and Amighian, J., Magnetic properties of ultrafine $MnFe_2O_4$ powders prepared by mechanochemical processing. *Physical Review B*, **2001**, *63*, p.184414.

[21] Nathani, H., Gubbala, S. and Misra, R.D.K., Magnetic behavior of nanocrystalline nickel ferrite: Part I. The effect of surface roughness. *Materials Science and Engineering: B*, **2005**, *121*, 126-136.

[22] Nathani, H., Gubbala, S. and Misra, R.D.K., Magnetic behavior of nickel ferrite–polyethylene nanocomposites synthesized by mechanical milling process. *Materials Science and Engineering: B*, **2004**, *111*, 95-100.

[23] Kodama, R.H. and Berkowitz, A.E., Atomic-scale magnetic modeling of oxide nanoparticles. *Physical Review B*, **1999**, *59*, p.6321.

[24] Iglesias, O. and Labarta, A., Finite-size and surface effects in maghemite nanoparticles: Monte Carlo simulations. *Physical Review B*, **2001**, *63*., p.184416.

[25] Kim, B.H., Lee, N., Kim, H., An, K., Park, Y.I., Choi, Y., Shin, K., Lee, Y., Kwon, S.G., Na, H.B. and Park, J.G., Large-scale synthesis of uniform and extremely small-sized iron oxide nanoparticles for high-resolution T 1 magnetic resonance imaging contrast agents. *Journal of the American Chemical Society*, **2011**, *133*, 12624-12631.

[26] Gonzalez-Fernandez, M.A., Torres, T.E., Andrés-Vergés, M., Costo, R., De La Presa, P., Serna, C.J., Morales, M.P., Marquina, C., Ibarra, M.R. and Goya, G.F., Magnetic nanoparticles for power absorption: Optimizing size, shape and magnetic properties. *Journal of Solid State Chemistry*, **2009**, *182*, 2779-2784.

[27] Lv, Y., Yang, Y., Fang, J., Zhang, H., Peng, E., Liu, X., Xiao, W. and Ding, J., Size dependent magnetic hyperthermia of octahedral Fe 3 O 4 nanoparticles. *RSC advances*, **2015**, *5*, 76764-76771.

[28] Ma, M., Wu, Y., Zhou, J., Sun, Y., Zhang, Y. and Gu, N., Size dependence of specific power absorption of Fe_3O_4 particles in AC magnetic field. *Journal of Magnetism and Magnetic Materials*, **2004**, *268*, 33-39.

[29] Tong, S., Quinto, C.A., Zhang, L., Mohindra, P. and Bao, G., Size-dependent heating of magnetic iron oxide nanoparticles. *Acs Nano*, **2017**, *11*, 6808-6816.

[30] Wang, X., Gu, H. and Yang, Z., The heating effect of magnetic fluids in an alternating magnetic field. *Journal of magnetism and magnetic materials*, **2005**, *293,* 334-340.

[31] Yamamoto, Y., Horiuchi, K., Takeuchi, M., Tanaka, N., Aihara, R., Takeuchi, N. and Fujita, S., Size dependence study on magnetic heating properties of superparamagnetic iron oxide nanoparticles suspension. *Journal of Applied Physics*, **2014**, *116*, p.123906.

[32] Shirsath, S.E., Kadam, R.H., Gaikwad, A.S., Ghasemi, A. and Morisako, A., Effect of sintering temperature and the particle size on the structural and magnetic properties of nanocrystalline Li0. 5Fe2. 5O4. *Journal of magnetism and magnetic materials*, **2011**, *323*, 3104-3108.

[33] Kim, T. and Shima, M., Reduced magnetization in magnetic oxide nanoparticles. *Journal of applied physics*, **2007**, *101*, p.09M516.

[34] Hoffmann, R.C., Kaloumenos, M., Spiehl, D., Erdem, E., Repp, S., Weber, S. and Schneider, J.J., A microwave molecular solution based approach towards high-κ-tantalum (v) oxide nanoparticles: synthesis, dielectric properties and electron paramagnetic resonance spectroscopic studies of their defect chemistry. *Physical Chemistry Chemical Physics*, **2015**. *17,* 31801-31809.

[35] Hoffmann, R.C., Sanctis, S., Erdem, E., Weber, S. and Schneider, J.J., Zinc diketonates as single source precursors for ZnO nanoparticles: Microwave-assisted synthesis, electrophoretic deposition and field-effect transistor device properties. *Journal of Materials Chemistry C*, **2016**, *4*, 7345-7352.

[36] Repp, S., Harputlu, E., Gurgen, S., Castellano, M., Kremer, N., Pompe, N., Wörner, J., Hoffmann, A., Thomann, R., Emen, F.M. Weber, S., Ocakoglu. K., Erdem, E., Synergetic effects of Fe^{3+} doped spinel Li_4 Ti_5 O_{12} nanoparticles on reduced graphene oxide for high surface electrode hybrid supercapacitors. *Nanoscale*, **2018**, *10*, 1877-1884.

[37] Bateni, A., Repp, S., Thomann, R., Acar, S., Erdem, E. and Somer, M., Defect structure of ultrafine MgB_2 nanoparticles. *Applied Physics Letters*, **2014**, *105*, p.202605.

[38] Öztuna, E., Ünal, Ö., Erdem, E., Yağcı Acar, H. and Ünal, U., Layer-by-layer grown electrodes composed of cationic Fe3O4 nanoparticles and graphene oxide nanosheets for electrochemical energy storage devices. *Journal of Physical Chemistry C*, **2019**, *123*, 3393-3401.

[39] Erdem, E., Electron beam curing of $CoFe_2O_4$ nanoparticles. *Hybrid Materials*, **2014**, *1*, 62-70.

[40] Asgari, M., Soleymani, M., Miri, T. and Barati, A., A robust method for fabrication of monodisperse magnetic mesoporous silica nanoparticles with core-shell structure as anticancer drug carriers. *Journal of Molecular Liquids*, **2019**, *292*, p.111367.

[41] Asgari, M., Soleymani, M., Miri, T. and Barati, A., Design of thermosensitive polymer-coated magnetic mesoporous silica nanocomposites with a core-shell-shell structure as a magnetic/temperature dual-responsive drug delivery vehicle. *Polymers for Advanced Technologies*, **2021**, *32*, 4101-4109.

[42] Shaterabadi, Z., Nabiyouni, G. and Soleymani, M., Correlation between effects of the particle size and magnetic field strength on the magnetic hyperthermia efficiency of dextran-coated magnetite nanoparticles. *Materials Science and Engineering: C*, **2020**, *117*, p.111274.

[43] Wu, W., He, Q. and Jiang, C., Magnetic iron oxide nanoparticles: synthesis and surface functionalization strategies. *Nanoscale research letters*, **2008**, *3*, 397-415.

[44] Lu, W., Ling, M., Jia, M., Huang, P., Li, C. and Yan, B., Facile synthesis and characterization of polyethylenimine-coated Fe3O4 superparamagnetic nanoparticles for cancer cell separation. *Molecular medicine reports*, **2014**, *9*, 1080-1084.

[45] Liu, F., Cao, P.J., Zhang, H.R., Tian, J.F., Xiao, C.W., Shen, C.M., Li, J.Q. and Gao, H.J., Novel nanopyramid arrays of magnetite. *Advanced materials*, **2005**, *17*, 1893-1897.

[46] Shaterabadi, Z., Nabiyouni, G. and Soleymani, M., High impact of in situ dextran coating on biocompatibility, stability and magnetic properties of iron oxide nanoparticles. *Materials Science and Engineering: C*, **2017**, *75*, 947-956.

[47] Shaterabadi, Z., Nabiyouni, G. and Soleymani, M., Optimal size for heating efficiency of superparamagnetic dextran-coated magnetite nanoparticles for application in magnetic fluid hyperthermia. *Physica C: Superconductivity and its Applications*, **2018**, *549*, 84-87.

[48] Kotoulas, A., Dendrinou-Samara, C., Angelakeris, M. and Kalogirou, O., The effect of polyol composition on the structural and magnetic properties of magnetite nanoparticles for magnetic particle hyperthermia. *Materials*, **2019**, *12*, p.2663.

[49] Mürbe, J., Rechtenbach, A. and Töpfer, J., Synthesis and physical characterization of magnetite nanoparticles for biomedical applications. *Materials Chemistry and Physics*, **2008**, *110*, 426-433.

[50] Gnanaprakash, G., Philip, J., Jayakumar, T. and Raj, B., Effect of digestion time and alkali addition rate on physical properties of magnetite nanoparticles. *The Journal of Physical Chemistry B*, **2007**, *111*, 7978-7986.

[51] Cullity, B.D. and Graham, C.D., *Introduction to magnetic materials*. **2011**, John Wiley & Sons.

[52] Chaki, S.H., Malek, T.J., Chaudhary, M.D., Tailor, J.P. and Deshpande, M.P., Magnetite Fe3O4 nanoparticles synthesis by wet chemical reduction and their characterization. *Advances in Natural Sciences: Nanoscience and Nanotechnology*, **2015**, *6*, p.035009.

[53] Chen, J.P., Sorensen, C.M., Klabunde, K.J., Hadjipanayis, G.C., Devlin, E. and Kostikas, A., Size-dependent magnetic properties of $MnFe_2O_4$ fine particles synthesized by coprecipitation. *Physical review B*, **1996**, *54*, p.9288.

[54] Zheng, M., Wu, X.C., Zou, B.S. and Wang, Y.J., Magnetic properties of nanosized $MnFe_2O_4$ particles. *Journal of magnetism and magnetic materials*, **1998**, *183*, 152-156.

[55] Liu, C. and Zhang, Z.J., Size-dependent superparamagnetic properties of Mn spinel ferrite nanoparticles synthesized from reverse micelles. *Chemistry of Materials*, **200**1, *13*, 2092-2096.

[56] Grigorova, M., Blythe, H.J., Blaskov, V., Rusanov, V., Petkov, V., Masheva, V., Nihtianova, D., Martinez, L.M., Munoz, J.S. and Mikhov, M., Magnetic properties and Mössbauer spectra of nanosized $CoFe_2O_4$ powders. *Journal of magnetism and magnetic materials*, **1998**, *183*, 163-172.

[57] Jiang, J.Z., Goya, G.F. and Rechenberg, H.R., Magnetic properties of nanostructured $CuFe_2O_4$. *Journal of Physics: Condensed Matter*, **1999**, *11*, p.4063.

[58] Caruntu, D., Caruntu, G. and O'Connor, C.J., Magnetic properties of variable-sized Fe_3O_4 nanoparticles synthesized from non-aqueous homogeneous solutions of polyols. *Journal of physics D: Applied physics*, **2007**, *40*, p.5801.

[59] Brown Jr, W.F., Theory of the approach to magnetic saturation. *Physical Review*, **1940**, *58*, p.736.

[60] Martinez-Boubeta, C., Simeonidis, K., Makridis, A., Angelakeris, M., Iglesias, O., Guardia, P., Cabot, A., Yedra, L., Estradé, S., Peiró, F. and Saghi, Z., Learning from nature to improve the

heat generation of iron-oxide nanoparticles for magnetic hyperthermia applications. *Scientific reports*, **2013**, *3*, 1-8.

[61] Jin, Z.Q., Tang, W., Zhang, J.R., Qin, H.X. and Du, Y.W., Effective magnetic anisotropy of nanocrystalline Nd-Fe-Ti-N hard magnetic alloys. *The European Physical Journal B-Condensed Matter and Complex Systems*, **1998**, *3*, 41-44.

[62] Andreev, S.V., Bartashevich, M.I., Pushkarsky, V.I., Maltsev, V.N., Pamyatnykh, L.A., Tarasov, E.N., Kudrevatykh, N.V. and Goto, T., Law of approach to saturation in highly anisotropic ferromagnets Application to Nd-Fe-B melt-spun ribbons. *Journal of alloys and compounds*, **1997**, *260*, 196-200.

[63] Sarkar, D. and Mandal, M., Static and dynamic magnetic characterization of DNA-templated chain-like magnetite nanoparticles. *The Journal of Physical Chemistry C*, **2012**, *116*, 3227-3234.

[64] Engelmann, U.M., Seifert, J., Mues, B., Roitsch, S., Ménager, C., Schmidt, A.M. and Slabu, I., Heating efficiency of magnetic nanoparticles decreases with gradual immobilization in hydrogels. *Journal of Magnetism and Magnetic Materials*, **2019**, *471*, 486-494.

[65] Carrey, J., Mehdaoui, B. and Respaud, M., Simple models for dynamic hysteresis loop calculations of magnetic single-domain nanoparticles: Application to magnetic hyperthermia optimization. *Journal of Applied Physics*, **2011**, *109*, p.083921.

[66] Dennis, C.L. and Ivkov, R., Physics of heat generation using magnetic nanoparticles for hyperthermia. *International Journal of Hyperthermia*, **2013**, *29*, 715-729.

[67] Goya, G.F. and Morales, M.P., Field dependence of blocking temperature in magnetite nanoparticles. *Journal of Metastable and Nanocrystalline Materials,* **2004**, *20*, 673-678.

[68] Kechrakos, D. and Trohidou, K.N., Competition between dipolar and exchange interparticle interactions in magnetic nanoparticle films. *Journal of magnetism and magnetic materials*, **2003**, *262*, 107-110.

[69] Pauly, M., Pichon, B.P., Panissod, P., Fleutot, S., Rodriguez, P., Drillon, M. and Begin-Colin, S., Size dependent dipolar interactions in iron oxide nanoparticle monolayer and multilayer Langmuir–Blodgett films. *Journal of Materials Chemistry*, **2012**, *22*, 6343-6350.

[70] Bødker, F., Mørup, S. and Linderoth, S., Surface effects in metallic iron nanoparticles. *Physical review letters*, **1994**, *72*, p.282.

[71] Bartolomé, J., García, L.M., Bartolomé, F., Luis, F., López-Ruiz, R., Petroff, F., Deranlot, C., Wilhelm, F., Rogalev, A., Bencok, P. and Brookes, N.B., Magnetic polarization of noble metals

by Co nanoparticles in M-capped granular multilayers (M= Cu, Ag, and Au): An x-ray magnetic circular dichroism study. *Physical Review B*, **2008**, *77*, p.184420.

[72] Luis, F., Torres, J.M., García, L.M., Bartolomé, J., Stankiewicz, J., Petroff, F., Fettar, F., Maurice, J.L. and Vaures, A., Enhancement of the magnetic anisotropy of nanometer-sized Co clusters: Influence of the surface and of interparticle interactions. *Physical Review B*, **2002**, *65*, p.094409.

[73] Gorenstein, M.I. and Greiner, W., Linear chains of dipoles and magnetic susceptibility. *Modern Physics Letters B*, **2014**, *28*, p.1450039.

[74] Anand, M., Hysteresis in a linear chain of magnetic nanoparticles. *Journal of Applied Physics*, **2020**, *128*, p.023903.

[75] Butter, K., Bomans, P.H.H., Frederik, P.M., Vroege, G.J. and Philipse, A.P., Direct observation of dipolar chains in iron ferrofluids by cryogenic electron microscopy. *Nature materials*, **2003**, *2*, 88-91.

[76] Morales, I., Costo, R., Mille, N., Da Silva, G.B., Carrey, J., Hernando, A. and De la Presa, P., High frequency hysteresis losses on γ-Fe_2O_3 and Fe_3O_4: susceptibility as a magnetic stamp for chain formation. *Nanomaterials*, **2018**, *8*, p.970.

[77] Myrovali, E., Maniotis, N., Makridis, A., Terzopoulou, A., Ntomprougkidis, V., Simeonidis, K., Sakellari, D., Kalogirou, O., Samaras, T., Salikhov, R. and Spasova, M., Arrangement at the nanoscale: Effect on magnetic particle hyperthermia. *Scientific reports*, **2016**, *6*, 1-11.

Captions for Tables:

Table 1 Synthesis conditions, TEM particle size, and some characteristics of the DM NPs

Table 2 The calculated K_{eff} values of the DM NPs.

Table 1 Synthesis conditions, TEM particle size, and some characteristics of the DM NPs

Sample	Synthesis conditions+	D (nm)	M_s (emu/$g_{Dex\text{-}M}$)	m_r (%)	M_s^* (emu/$g_{Dex\text{-}M}$)	M_s^{**} (emu/g_{Mag})
DM3	Co 80℃	3.1±0.4	8.3	60.73	9.9	16.3
DM5	Co80ºC+Hy120ºC	4.5±0.4	26.5	72.66	27.9	38.4
DM7	Co80ºC+Hy140ºC	6.7±0.3	33.8	80.60	34.9	43.3
DM8	Co80ºC+Hy160ºC	8.1±0.2	44.4	82.21	45.3	55.1
DM11	Co80ºC+Hy180ºC	11.5±0.2	59.2	82.62	59.9	72.5
DM15	Co80ºC+Hy200ºC	15.0±0.3	64	86.38	64.7	74.9
DM19	Co80ºC+Hy220ºC	18.9±0.3	67.9	87.69	68.4	78.0

+ Co-precipitation and hydrothermal synthesis methods are respectively written as Co and Hy for short. The synthesis temperatures are also written next to each synthesis method.

Table 2 The calculated K_{eff} values of the DM NPs.

Sample DMx	DM3	DM5	DM7	DM8	DM11	DM15	DM19
K_{eff} ($\times 10^5$ J/m^3)	8.03	4.57	1.92	1.44	0.89	0.97	0.45

Captions for Figures:

Fig. 1 TEM images of the DM NPs. The corresponding size distribution histograms and the lognormal fits are shown in the inset of the TEM images.

Fig. 2 SEM images of the DM19 NPs with two different resolutions

Fig. 3 XRD spectra of the DM NPs, indicating their characteristic peaks

Fig. 4 Initial magnetization curves of the DM NPs as a function of applied magnetic field, obtained from the saturated hysteresis loops.

Fig. 5 The plot of the cube root of the saturation magnetization ($\mathrm{M_s^{**}}^{1/3}$) versus the inverse of the average diameter ($1/\mathrm{D}$) of the DM NPs. The circles and the solid line show the experimental data and a linear fit to them, respectively.

Fig. 6 The plot of the effective anisotropy ($\mathrm{K_{eff}}$) vs. 1/D data of the DM NPs. The circles and the solid line respectively show the calculated values and a linear fit to them using (a) Eq. (5) and (b) Eq. (6).

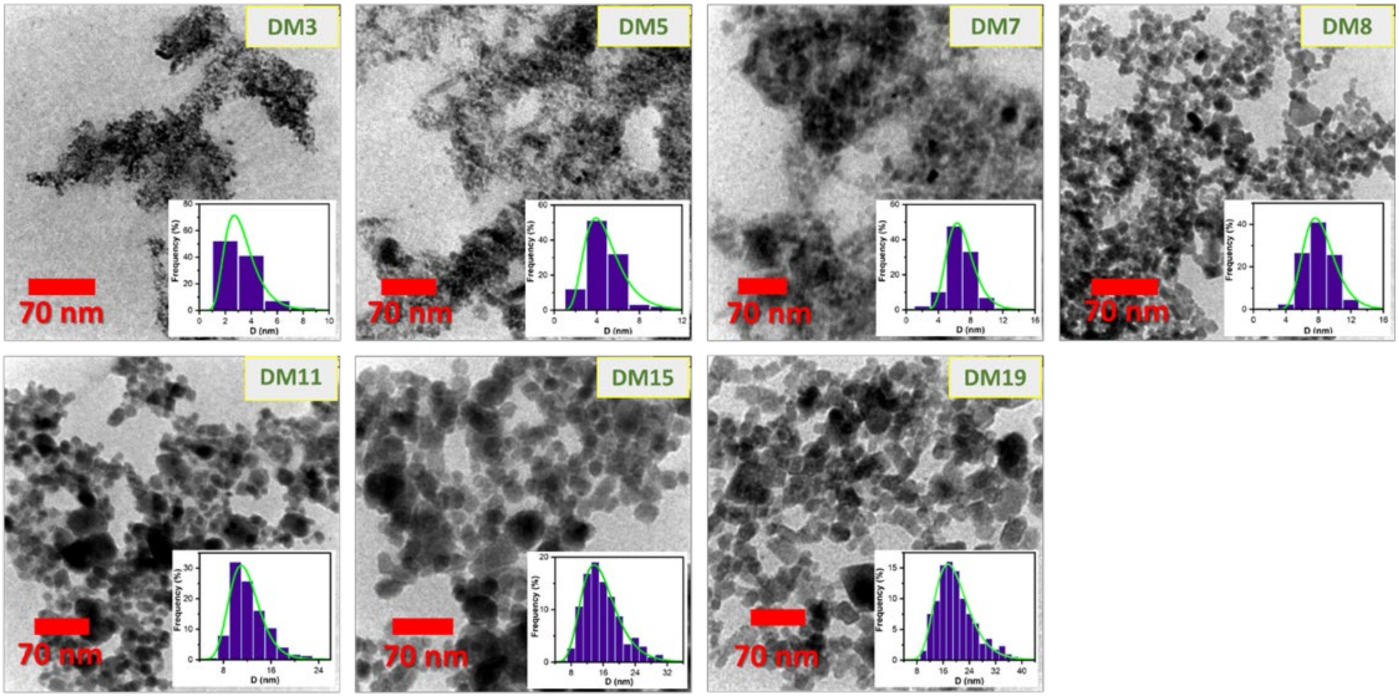

Fig. 1 TEM images of the DM NPs. The corresponding size distribution histograms and the lognormal fits are shown in the inset of the TEM images.

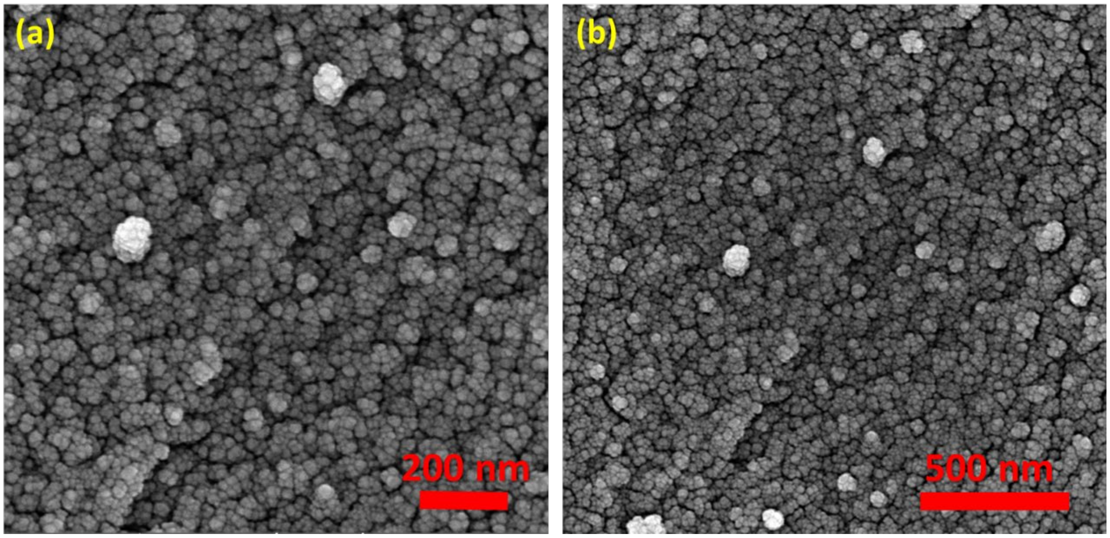

Fig. 2 SEM images of the DM19 NPs with two different resolutions

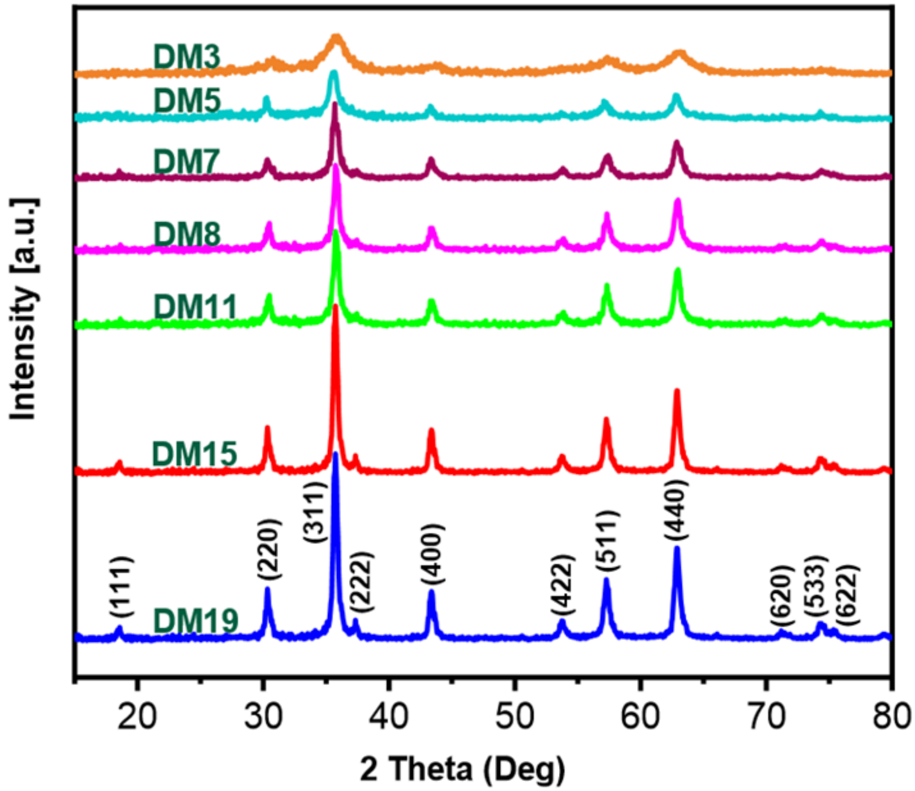

Fig. 3 XRD spectra of the DM NPs, indicating their characteristic peaks.

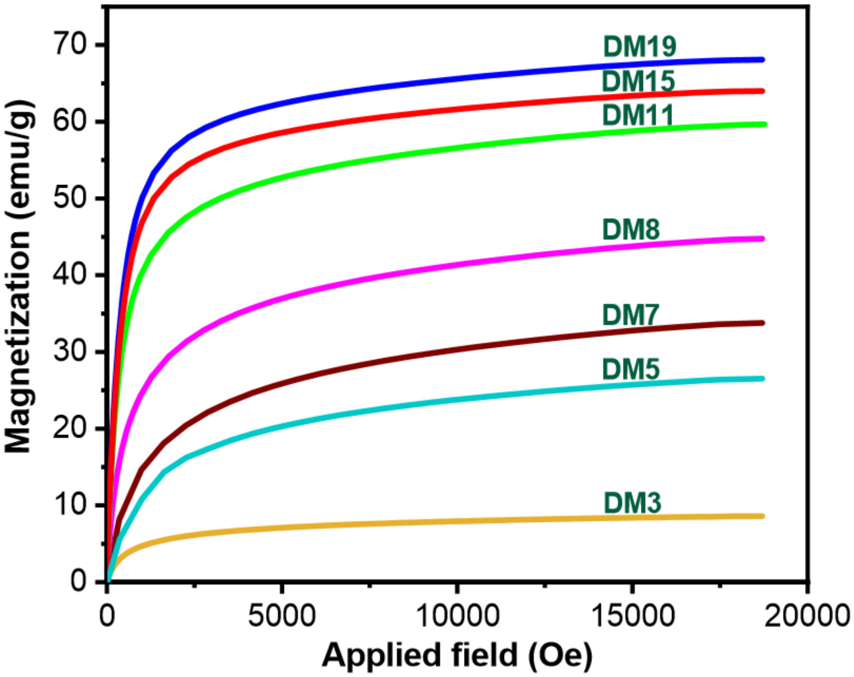

Fig. 4 Initial magnetization curves of the DM NPs as a function of applied magnetic field, obtained from the saturated hysteresis loops.

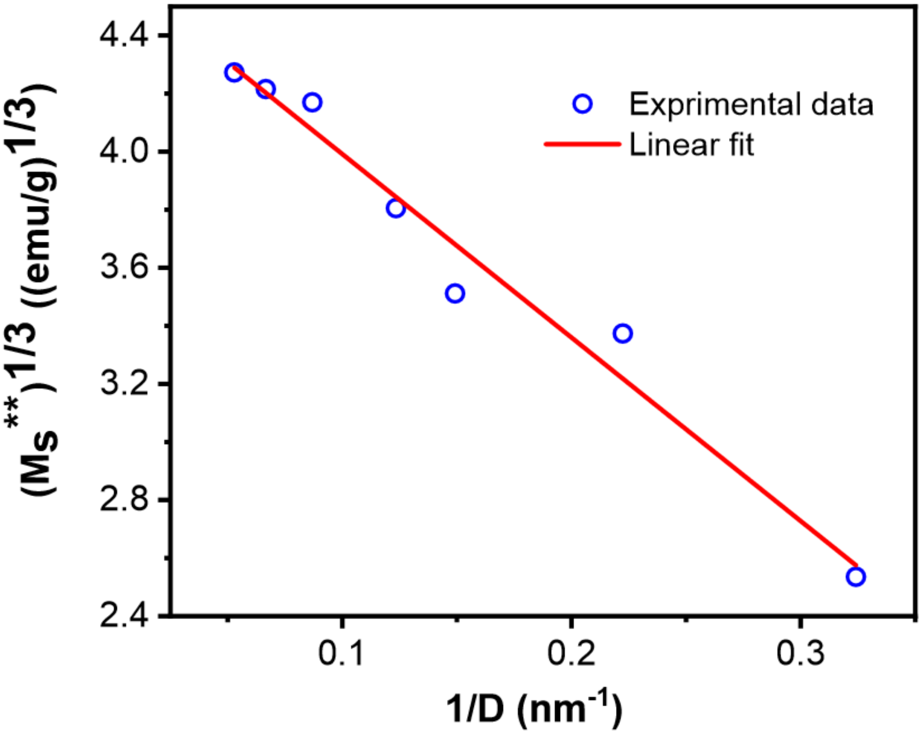

Fig. 5 The plot of the cube root of the saturation magnetization ($M_s^{**1/3}$) versus the inverse of the average diameter ($1/D$) of the DM NPs. The circles and the solid line show the experimental data and a linear fit to them, respectively.

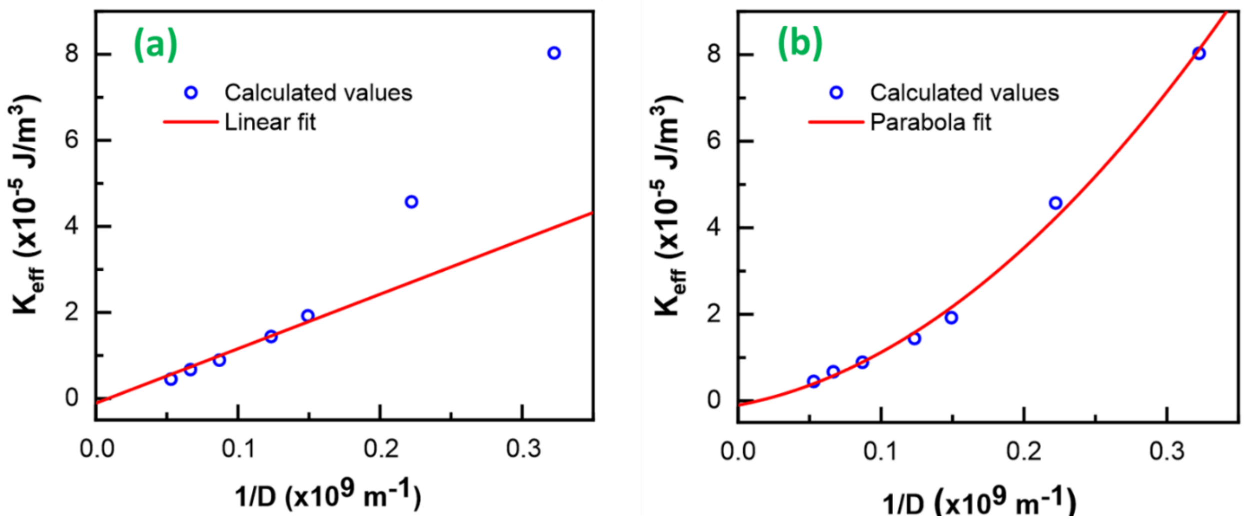

Fig. 6 The plot of the effective anisotropy (K_{eff}) vs. 1/D data of the DM NPs. The circles and the solid line respectively show the calculated values and a linear fit to them using (a) Eq. (5) and (b) Eq. (6).

Graphical abstract